

Key Points:

- We performed shock recovery experiments with granite and spherically decaying compressive waves; numerical models constrain peak pressures
- Shocked granite samples are found to retain pre-impact stratigraphy and to document shock-stage transitions between <0.5 and ~18 GPa
- Shear-induced melting of granite at bulk peak pressures as low as 6 GPa; stishovite nucleated as a liquidus phase in melt veins at >10 GPa

Supporting Information:

Supporting Information may be found in the online version of this article.

Correspondence to:

C. Hamann,
christopher.hamann@mfh.berlin

Citation:

Hamann, C., Kurosawa, K., Ono, H., Tada, T., Langenhorst, F., Pollok, K., et al. (2023). Experimental evidence for shear-induced melting and generation of stishovite in granite at low (<18 GPa) shock pressure. *Journal of Geophysical Research: Planets*, 128, e2023JE007742. <https://doi.org/10.1029/2023JE007742>

Received 5 JAN 2023
Accepted 17 MAY 2023










Author Contributions:

Conceptualization: Christopher Hamann, Kosuke Kurosawa, Takafumi Matsui
Data curation: Christopher Hamann, Kosuke Kurosawa
Formal analysis: Christopher Hamann, Kosuke Kurosawa, Haruka Ono, Toshihiro Tada, Falko Langenhorst, Kilian Pollok, Hidenori Genda, Takafumi Niihara, Takaya Okamoto, Takafumi Matsui

© 2023 The Authors.

This is an open access article under the terms of the [Creative Commons Attribution-NonCommercial License](#), which permits use, distribution and reproduction in any medium, provided the original work is properly cited and is not used for commercial purposes.

Experimental Evidence for Shear-Induced Melting and Generation of Stishovite in Granite at Low (<18 GPa) Shock Pressure

Christopher Hamann¹ , Kosuke Kurosawa² , Haruka Ono² , Toshihiro Tada³ , Falko Langenhorst⁴ , Kilian Pollok⁴ , Hidenori Genda⁵ , Takafumi Niihara⁶ , Takaya Okamoto² , and Takafumi Matsui^{2,3,†}

¹Museum für Naturkunde Berlin, Berlin, Germany, ²Planetary Exploration Research Center, Chiba Institute of Technology, Chiba, Japan, ³Institute for Geo-Cosmology, Chiba Institute of Technology, Chiba, Japan, ⁴Friedrich-Schiller-Universität Jena, Analytische Mineralogie der Mikro- und Nanostrukturen, Jena, Germany, ⁵Earth-Life Science Institute, Tokyo Institute of Technology, Tokyo, Japan, ⁶Department of Applied Sciences, Okayama University of Science, Okayama, Japan

Abstract Knowledge of the shock behavior of planetary materials is essential to interpret shock metamorphism documented in rocks at hypervelocity impact structures on Earth, in meteorites, and in samples retrieved in space missions. Although our understanding of shock metamorphism has improved considerably within the last decades, the effects of friction and plastic deformation on shock metamorphism of complex, polycrystalline, non-porous rocks are poorly constrained. Here, we report on shock-recovery experiments in which natural granite was dynamically compressed to 0.5–18 GPa by singular, hemispherically decaying shock fronts. We then combine petrographic observations of shocked samples that retained their pre-impact stratigraphy with distributions of peak pressures, temperatures, and volumetric strain rates obtained from numerical modeling to systematically investigate progressive shock metamorphism of granite. We find that the progressive shock metamorphism of granite observed here is mainly consistent with current classification schemes. However, we also find that intense shear deformation during shock compression and release causes the formation of highly localized melt veins at peak pressures as low as 6 GPa, which is an order of magnitude lower than currently thought. We also find that melt veins formed in quartz grains compressed to >10–12 GPa contain the high-pressure silica polymorph stishovite. Our results illustrate the significance of shear and plastic deformation during hypervelocity impact and bear on our understanding of how melt veins containing high-pressure polymorphs form in moderately shocked terrestrial impactites or meteorites.

Plain Language Summary When asteroids, comets, or smaller fragments thereof impact the solid surfaces of planets, moons, or other asteroids, the rocks they strike undergo sudden and irreversible changes while an impact crater forms. These material changes are called shock metamorphism and result from the extremely high pressures, temperatures, and deformation rates caused by the impact. However, the role of rapid shear deformation on impact heating and shock metamorphism is poorly understood. Using a novel experimental setup, we performed shock-wave experiments with granite, a naturally occurring rock, that allows us to study the role of extreme deformation rates during impact-crater formation. Furthermore, our experimental setup allows us to avoid several pitfalls such as excavation and ejection of shocked material from a growing impact crater or multiple reflections of shock waves at sample containers that typically plagued previous experiments. We find that intense shear deformation during crater formation results in significant but highly localized heating. This additional heating causes melting of granite at shock pressures as low as 6 GPa, which is about 10 times less than currently thought. Our findings may explain how thin melt veins often observed in shock-metamorphosed meteorites or rocks sampled from terrestrial impact craters have formed.

1. Introduction

Impact cratering is among the most dominant geological processes that shape and modify planetary crusts. To understand planetary crustal evolution and to interpret observations of planetary surfaces via remote-sensing techniques, knowledge of the dynamic response of planetary materials to hypervelocity impacts of asteroids or comets is therefore crucial. Such knowledge is also needed to interpret shock metamorphism of rocks sampled at terrestrial impact structures or to understand shock metamorphism in meteorites and extraterrestrial material retrieved in sample-return missions.

Funding acquisition: Kosuke Kurosawa, Takafumi Matsui

Investigation: Christopher Hamann, Kosuke Kurosawa, Haruka Ono, Toshihiro Tada, Falko Langenhorst, Kilian Pollok, Takafumi Niihara, Takaya Okamoto

Methodology: Kosuke Kurosawa

Resources: Christopher Hamann, Kosuke Kurosawa, Falko Langenhorst

Software: Kosuke Kurosawa, Hidenori Genda

Supervision: Christopher Hamann, Kosuke Kurosawa

Validation: Christopher Hamann, Kosuke Kurosawa

Visualization: Christopher Hamann, Kosuke Kurosawa

Writing – original draft: Christopher Hamann

Writing – review & editing: Kosuke Kurosawa, Haruka Ono, Toshihiro Tada, Falko Langenhorst, Kilian Pollok, Hidenori Genda, Takafumi Niihara, Takaya Okamoto, Takafumi Matsui

Laboratory shock-wave experiments have been essential in characterizing the dynamic response of planetary materials to shock compression and subsequent release (e.g., De Carli & Milton, 1965; Ebert et al., 2013; Hörz et al., 2005; Kowitz et al., 2013; Kraus et al., 2012; Kurosawa et al., 2012; Milton & De Carli, 1963; Schaal & Hörz, 1977; R. T. Schmitt, 2000; Stöffler & Langenhorst, 1994; Tracy et al., 2020) and in characterizing their properties at high pressure and temperature conditions of deep planetary interiors (e.g., Millot et al., 2015). Samples recovered from shock-wave experiments also provide insight into shock metamorphism of solids (e.g., Langenhorst & Deutsch, 2012; Miyahara et al., 2021; Sharp & De Carli, 2006; Stöffler & Langenhorst, 1994) and are therefore the basis of classification schemes of progressive shock metamorphism (e.g., Stöffler & Langenhorst, 1994; Stöffler et al., 1991, 2018). Such schemes typically define “shock stages” that link petrographic observations of specific shock effects such as plastic deformation, phase transformations, or melting to specific shock-pressure ranges. These are consulted to interpret the possible shock-metamorphic overprint documented in a given rock or mineral sample. However, the recovery of shocked material that documents in one single sample large shock-pressure ranges that cover multiple shock stages as well as the transitions between them has so far been challenging in experiments. On the one hand, shock-recovery experiments using metal flyer plates and shock-wave reverberation or “ring-up” setups (e.g., Bell, 2016; Kenkmann et al., 2000; Langenhorst & Deutsch, 1994; Ogilvie et al., 2011; R. T. Schmitt, 2000; Stöffler & Langenhorst, 1994; Tomeoka et al., 1999) typically compress a sample to a well-defined, but rather narrow peak-pressure range. Impact-cratering experiments with two-stage light-gas guns, on the other hand, are typically afflicted with the excavation of shocked material from the growing transient crater, which makes the reconstruction of the pre-impact positions and therefore the peak pressures and temperatures experienced in specific parts of the target challenging (e.g., Wünnemann et al., 2016). With some exceptions (e.g., Hamann et al., 2016; Kohout et al., 2020; Kurosawa et al., 2022; Nagaki et al., 2016), direct transitions between shock stages that form as a result of a continuously decaying shock wave have therefore rarely been studied. Excavation of fragmented and brecciated material in cratering experiments also makes it difficult to assess the amount and mode of local shear-induced melting at bulk peak pressures far below those typically required for incipient melting (e.g., Kenkmann et al., 2000; Langenhorst et al., 2002). This process is held to cause the formation of melt veins in moderately shocked meteorites (e.g., Hu & Sharp, 2022; Langenhorst & Poirier, 2000; Sharp & De Carli, 2006), yet how it operates on the scale of individual grains in complex, non-porous, polymineralic rocks is poorly understood.

Here, we report on shock-recovery experiments with a recently developed technique (Kurosawa et al., 2022; Ono et al., 2023) that allows us to produce a single hemispherical shock wave in a rock sample that can be fully recovered (i.e., ejection of material is suppressed). As outlined here, the recovered samples document a continuum of shock stages that form as a result of successively decreasing peak pressures as the shock wave decays. Furthermore, the samples experienced singular shock compression as opposed to multiple reflections of compressive waves at metal containers in shock-reverberation experiments as well as a large degree of shear deformation and fragmentation that is typical for hypervelocity impacts in nature (e.g., Collins et al., 2004; Grady, 1980). As shown here, this results in the formation of melt veins in otherwise only moderately shocked material.

In this study, we focus on granite as an analog material for typical differentiated silica-rich crustal rocks. Granites are among the most abundant rocks in the Earth's upper continental crust and have therefore been frequent targets of hypervelocity impacts, as exemplified by many impact structures formed in granitoid targets (Osinski et al., 2022). In addition, interest in the shock metamorphism of granite has recently been rekindled by the joint International Ocean Discovery Program and International Continental Scientific Drilling Program Expedition 364 drilling into the granitoid peak ring of the Chicxulub impact structure (e.g., Ebert et al., 2020, 2021; Rae et al., 2019; Riller et al., 2018). Although the crusts of the other terrestrial planets and differentiated asteroids are typically basaltic in composition, granitoid clasts in lunar meteorites (Zeng et al., 2021) or chondrites (Terada & Bischoff, 2009) and recently discovered silica-rich achondrites like Northwest Africa 11119 (Srinivasan et al., 2018) or Erg Chech 002 (e.g., Barrat et al., 2021) suggest that silica-rich magmatism existed in the early solar system as well. This magmatism could have formed silica-rich crusts on differentiated planetesimals that were later destroyed by collisions. Understanding the evolution of planetary crusts and interpretation of shock metamorphism recorded in terrestrial or extraterrestrial granitoid samples therefore requires knowledge of the processes and products of hypervelocity impacts on granitoid rocks.

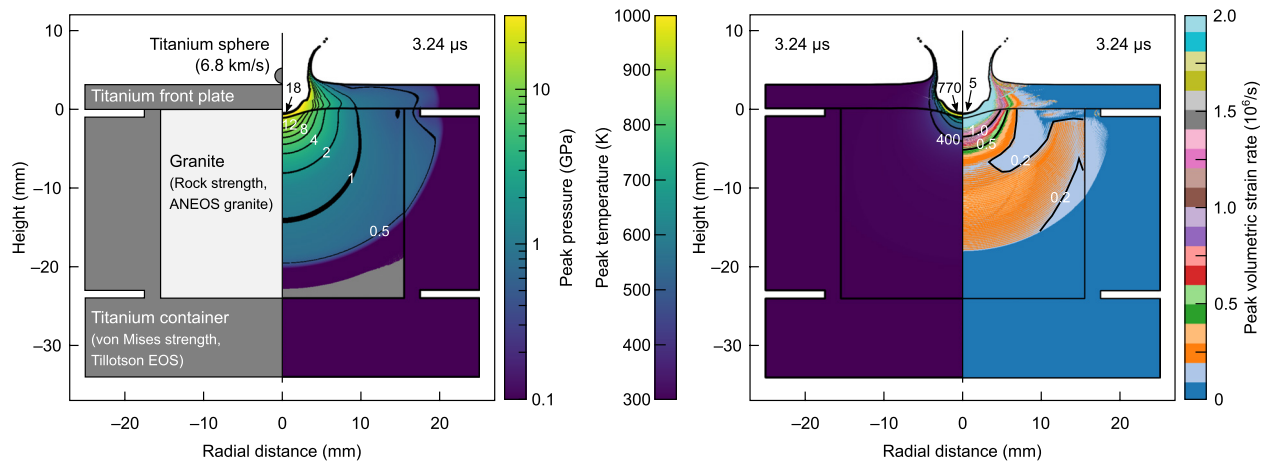


Figure 1. Overview of the experimental setup and distribution of peak pressure, temperature, and volumetric strain rate for experiment #494, as calculated from the iSALE model. The model snapshots are taken at 3.24 μs after impact, which is the time step that best reproduces the geometric shape and curvature of the recovered sample close to the point of impact (cf. Figures 2 and 3). Numbers close to the transient crater (arrows) denote peak values.

2. Materials and Methods

2.1. Materials and Experimental Setup

We conducted impact experiments with Inada granite from the Ibaraki prefecture in Japan using a two-stage light-gas gun at Planetary Exploration Research Center, Chiba Institute of Technology, Japan. Samples of Inada granite were shaped into cylinders of 30 mm diameter and 24 mm height (Figures S1a and S1b in Supporting Information S1). Inada granite used here consists of about 31 vol.% quartz; 28 vol.% plagioclase with normal zoning ranging from rare, patchy calcic ($\text{An}_{79}\text{Ab}_{21}\text{Or}_0$) cores or homogeneous calcic ($\text{An}_{50}\text{Ab}_{49}\text{Or}_1$) cores over sodic intermediate regions ($\text{An}_{24}\text{Ab}_{74}\text{Or}_2$) to sodic rims ($\text{An}_5\text{Ab}_{94}\text{Or}_1$); 25 vol.% alkali feldspar ($\text{An}_0\text{Ab}_{10}\text{Or}_{90}$); 15 vol.% biotite; and 1 vol.% accessories such as zircon and apatite. The granite has a coarse-grained magmatic fabric with virtually no porosity (Figure S2 in Supporting Information S1) and large quartz and feldspar grains ($\sim 3 \pm 1$ mm), smaller biotite grains (~ 1 mm), and volumetrically insignificant accessory zircon and apatite (< 0.2 mm). The granite's bulk composition and the compositions of the feldspars and of biotite are given in Table S1 in Supporting Information S1.

We used the same experimental setup as that of Kurosawa et al. (2022) and Ono et al. (2023) and therefore only briefly describe key setups here. Ejection of shocked material was prevented and recovery of shocked samples that retain their pre-impact stratigraphy was facilitated by inserting the granite cylinders into cylindrical titanium containers that were covered by detachable 3-mm-thick titanium plates. Spherical projectiles made from either titanium (2 mm diameter; experiment #494) or polycarbonate (4.8 mm diameter; experiment #505) were shot onto the titanium cover plates at 6.80 and 5.83 km s^{-1} , respectively. Schematic illustrations of the experimental setups of experiments #494 and #505 are given in Figure 1 and Figure S3 in Supporting Information S1, respectively. Details on the experimental conditions are summarized in Table 1.

Because the diameters of the projectiles used here are much smaller than the dimensions of the granite cylinders, the isobaric core (e.g., Pierazzo et al., 1997; Rae et al., 2021) produced in a granite sample is also much smaller than the sample itself. This results in an expanding, hemispherical shock wave that continuously decays with

Table 1
Overview of Experimental Conditions

Experiment	Projectile	Projectile mass (mg)	Projectile diameter (mm)	Impact velocity (km/s)	Thickness of titanium front plate (mm)	Peak pressure ^a (GPa)
494	Titanium	18.70	2.0	6.80	3	18 ± 1
505	Polycarbonate	67.86	4.8	5.83	3	11 ± 1

^aAverage peak pressure at the sample surface immediately beneath the point of impact on the titanium front plate as estimated from numerical simulation.

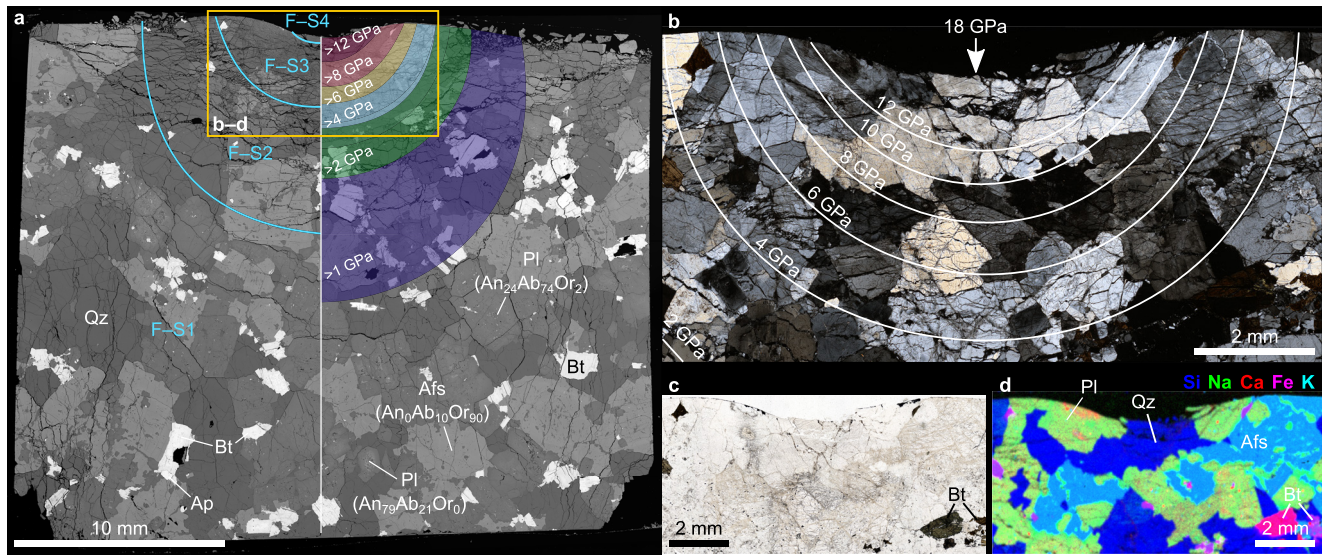


Figure 2. Shocked granite recovered from experiment #494. (a) Back-scattered electron (BSE) image of the entire thin section cut perpendicular to the impacted surface. Shock-pressure contours derived from the iSALE model (cf. Figure 1) as well as the approximate theoretical positions of the F-S1 to F-S4 shock stages defined by Stöffler et al. (2018) are superimposed onto the BSE image for reference. (b) Cross-polarized transmitted-light image of the impacted side; shock-pressure contours derived from the iSALE model are shown again for reference. (c) Linear-polarized transmitted-light image of the impacted side. (d) Micro X-ray fluorescence composite element distribution map of Si, Na, Ca, Fe, and K. Quartz (Qz) appears dark blue, plagioclase (Pl) green to orange, alkali feldspar (Afs) light blue, and biotite (Bt) as well as apatite (Ap) red to pink.

increasing distance. This shock-wave configuration differs from conventional shock-reverberation experiments that use large, planar metal (typically iron) flyer plates and planar compressive pulses. The latter engulf and compress in multiple reflections or “ring-up” steps the entire front side of a thin disc cut from a rock sample enclosed in a metal container. Although “ring-up” compression due to compressive pulses reflected at the interface between titanium plate and rock sample also exists in our setup, the reflected pulses are much weaker than in conventional shock-reverberation experiments because the isobaric core is much smaller than the sample and the shock front has significantly decayed upon arrival at the sample–container interface. In addition, the use of titanium results in only moderate shock impedance differences between the granite sample and the metal container. The effects of ring-up compression are therefore negligible in our setup (cf. Kurosawa et al., 2022). As ballistic ejection of sample material is suppressed by the titanium plate, and because peak pressures are mainly a function of distance (impedance mismatches among the dominant mineral phases in the granite—quartz, and feldspar—are small so that local pressure excursions will also be small; Text S1 and Figure S4 in Supporting Information S1), we can recover shocked samples that preserve their pre-impact stratigraphy and that should document a continuum of shock-metamorphic overprint as a function of pre-impact position. However, because peak pressures reached in our experiments cannot be calculated using conventional analytical methods such as one-dimensional impedance matching (Melosh, 1989), sophisticated shock physics codes as well as accurate equations of state for all materials involved are needed to estimate spatial and temporal distributions of peak pressures and temperatures in the granite targets (see subsequent section). The validity of the shock-physics modeling and the general experimental approach were confirmed in a previous study (Kurosawa et al., 2022) by employing stress gauges to directly measure the maximum principal stress at the point of impact and the far end of the sample.

2.2. Numerical Modeling

We conducted shock physics modeling to estimate spatial and temporal distributions of peak pressure and temperature in the shocked targets. The two-dimensional version of the iSALE shock physics code (Amsden et al., 1980; Ivanov et al., 1997; Wünnemann et al., 2006), iSALE-Dellen (Collins et al., 2016), was used here. The calculation settings and the employed material models were similar to those employed in Kurosawa et al. (2022) except that we used the Analytical Equation Of State (ANEOS, S. L. Thompson & Lauson, 1972) pertaining to granite (Pierazzo et al., 1997) for the granite cylinder. The “ROCK” model implemented into iSALE was used by combining the parameter set pertaining to granite (Collins et al., 2004; Rae et al., 2021). Lagrangian tracer particles were inserted into each computational cell. Peak pressures and temperatures experienced by the tracers were stored on

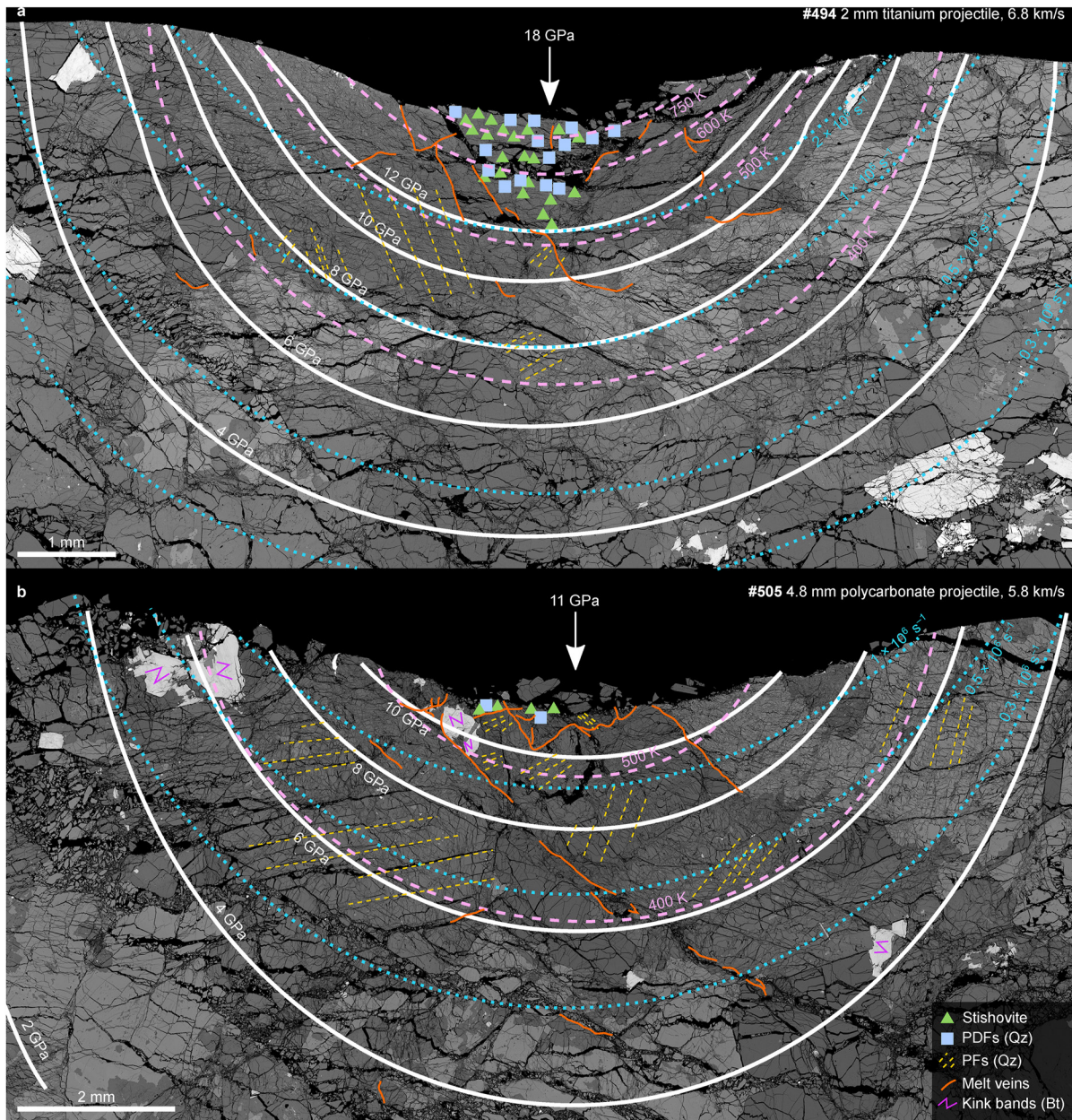


Figure 3. Detailed back-scattered electron (BSE) images of the impacted subsurfaces of granite cylinders recovered from experiments (a) #494 and (b) #505. The approximate distributions of peak pressure (white solid lines), temperature (pink dashed lines), and volumetric strain rate (turquoise stippled lines) from the iSALE models (cf. Figure 1 and Figure S2 in Supporting Information S1) as well as the spatial distributions of stishovite, planar deformation features and planar fractures in quartz (Qz), melt veins, and kink bands in biotite (Bt) are superimposed onto the BSE images for reference.

the tracer as well as temporal volumetric strain during the simulations. We then obtained the peak values of the volumetric strain rate during the simulation as an approximation of the position-dependent strain rate at the wave arrival. The input parameters of the material models and the calculation settings are summarized in Table S2 and S3 in Supporting Information S1 (for additional details and validation of the approach, cf. Kurosawa et al., 2022).

2.3. Analytical Techniques

Each sample was impregnated with epoxy resin while still positioned in the titanium container (Figures S1c and S1d in Supporting Information S1). The epoxy-hardened samples were cut in half in a direction parallel to the impact direction (i.e., perpendicular to the impacted surfaces; Figure S1 in Supporting Information S1).

Initial characterization of the reference sample and the shocked samples was performed prior to thin-section preparation using a Bruker M4 TORNADO PLUS micro X-ray fluorescence (μ XRF) spectrometer at Museum für Naturkunde Berlin, Germany. The bulk chemical composition of the granite (Table S1 in Supporting Information S1) was determined from a μ XRF element distribution map obtained from the reference sample using a 30 W rhodium X-ray tube that was operated without the use of a filter and at a sample chamber pressure of 1.7 mbar. The X-ray beam was focused to a spot size of 20 μ m (Mo-K α) on the sample surface by a polycapillary lens. The resulting X-ray spectra were simultaneously detected by two 30 mm² silicon-drift detectors with energy resolutions of ≤ 145 eV (Mn-K α) at 275 kcps pulse throughput. All element maps were obtained using a 50 kV acceleration voltage, a 600 μ A current, 20 μ m pixel resolution, and 5 ms dwell time per pixel.

Petrographic investigation of the recovered samples was done on thin sections by optical and scanning electron microscopy. Transmitted-light images were obtained using the Zeiss ZEN 3.5 software suite and a ZEISS Axiocam 712 color microscope camera coupled to a ZEISS Imager.M2 petrographic microscope at Museum für Naturkunde Berlin, Germany. Crystallographic orientations of planar lamellae in shocked quartz grains were measured under a petrographic microscope with a four-axis universal stage at Institute for Geo-Cosmology, Chiba Institute of Technology, Japan. Back-scattered electron (BSE) images were obtained from carbon-coated thin sections using a JEOL JXA-8500F field-emission electron microprobe at Museum für Naturkunde Berlin, Germany. Chemical compositions of the feldspars and biotite were obtained by wavelength-dispersive X-ray spectroscopy (WDS) using the same electron microprobe and an acceleration voltage of 15 kV, a beam current of 15 nA, and a beam diameter of 5 μ m. Count times on peak and background were 20 and 10 s, respectively, for Si, Ti, Al, Cr, Fe, Mn, Mg, and Ca and 10 and 5 s, respectively, for Na and K. Measured X-ray intensities were calibrated against reference minerals in the Smithsonian international standard suite. All analyses were processed by the ZAF routine in the JEOL series operating system to minimize matrix effects. Accuracy and reproducibility were checked before and after the analysis session by measurements of minerals of the Smithsonian standard suite. Detection limits for WDS are on the order of 0.02 wt.% for the elements considered here. Chemical compositions of glassy silicate veins were measured with energy-dispersive X-ray spectroscopy (EDS) using a Bruker XFlash 6110 X-ray spectrometer coupled to the electron microprobe. The use of EDS was dictated by the physical dimensions of the glass veins; specifically, freely adjustable measurement areas (instead of spherical spots obtained by defocusing of the electron beam) could be realized with the EDS detector. A 15 kV acceleration voltage, a 10 nA beam current, and 11 mm working distance were used for EDS and the electron beam was rasterized over areas with dimensions of typically 2×10 μ m or larger to prevent beam damage and loss of sodium from the glasses during analysis. Typical EDS detection limits for major elements were on the order of 0.2 wt.%.

Specific areas of interest identified in high-resolution BSE images were prepared for transmission electron microscopy (TEM) using a FEI Quanta 3D FEG focused ion beam (FIB) SEM instrument at Friedrich-Schiller-Universität Jena, Germany. This machine enabled the abrasion of the targeted area using a focused beam of Ga ions, monitored by secondary electron and BSE imaging. The Ga ion gun was operated at 30 kV with a beam current between 0.1 and 30 nA for sample preparation. A deposited Pt stripe was used to protect the surface. To remove amorphous layers on the FIB cut, the foils were cleaned at 5 kV using 48 pA beam current. Conventional bright-field (BF) and dark-field (DF) TEM images, selected area electron diffraction (SAED) patterns as well as high-angle annular dark-field scanning TEM (STEM) images were taken with a FEI Tecnai G2 FEG TEM operated at 200 keV using a double tilt holder.

3. Results

3.1. Peak Pressure, Temperature, and Strain-Rate Distributions

The numerical simulations of our experiments suggest that the peak pressures in the granite reached a maximum of about 18 GPa in experiment #494 (Figure 1) and 11 GPa in experiment #505 (Figure S3 in Supporting Information S1). Since natural granite consisting of several mineral phases of slightly different densities was used in the experiments, the actual peak pressure will vary slightly around this average value predicted from the granite ANEOS due to impedance differences (Ogilvie et al., 2011; Wittmann et al., 2021) between high-density phases (biotite and apatite) and phases of lower density (quartz and the feldspars). Using shock Hugoniot data for various relevant minerals as well as granite, we estimate using impedance matching methods an uncertainty in the average peak pressure of about $\pm 5\%$ close to the impacted surfaces (Text S1 and Figure S4 in Supporting Information S1). Successive attenuation of the compressive pulses resulted in hemispherical zones in which

peak pressures decreased within ~ 5.5 mm in experiment #494 and within ~ 6.8 mm in experiment #505 from the maximum shock pressure to about 3 GPa, which is the Hugoniot elastic limit of typical granite (e.g., Yuan & Prakash, 2013). Material at depths greater than 12 mm in experiment #494 and ~ 15 mm in experiment #505 was compressed to <1 GPa. The models further reveal that peak temperatures reached 770 K in experiment #494 (Figure 1) and 560 K in experiment #505 (Figure S3 in Supporting Information S1), which are well below the melting points of the volumetrically dominant phases (quartz and the feldspars) at 1 bar and dry conditions (e.g., Holland & Powell, 2001). The numerical simulations also suggest that peak volumetric strain rates reached $\sim 5 \times 10^6 \text{ s}^{-1}$ in experiment #494 (Figure 1) and $\sim 2 \times 10^6 \text{ s}^{-1}$ in experiment #505 (Figure S3 in Supporting Information S1) and then dropped rapidly with distance to between 0.1 and $0.3 \times 10^6 \text{ s}^{-1}$ at depths that correspond to about 3 GPa. Note that we present the peak values of the volumetric strain rate as first-order estimates as mentioned in Section 2.2 because strain rate has been frequently used to characterize shock wave experiments (e.g., Rae et al., 2022).

3.2. Spatial Distribution of Shock Effects

The peak-pressure and peak-temperature distributions obtained from the numerical models (Figure 1 and Figure S3 in Supporting Information S1) allow us to assign peak pressure and temperature ranges for specific regions in the thin sections. Here, we will use the calculated distributions superimposed onto the corresponding BSE-image mosaic of the entire section as shown in Figure 2 and Figure S5 in Supporting Information S1 as well as the impacted sub-surfaces in high resolution as shown in Figure 3 to estimate the peak pressure and temperature ranges at which specific shock effects appear in the thin sections. As the most drastic changes in peak pressures and temperatures occur close to the impacted surfaces, we used the time steps in the models that best reproduced the curvatures and geometric shapes of the impacted surfaces. For experiment #494, the best match between model and experiment was found to be at $3.24 \mu\text{s}$ after impact; for experiment #505, a time step of $5.05 \mu\text{s}$ after impact was used. It should be noted here that the shocked materials were further displaced after these time steps in the simulations. This further movement of material could cause uncertainties in the peak pressure estimates due to slight position mismatches between the shocked samples and the numerical results. At the final stage of impact, the displacement would be compensated by an expansion to the free surface, resulting in a number of open cracks as observed in the shocked samples (Figures 2 and 3 and Figure S5 in Supporting Information S1). We did not continue the numerical integration to such late time steps due to the computational cost. However, as the order of the stratification in the shocked samples was retained after the experiments, the peak pressure distributions calculated using iSALE at the selected time steps can be used as a good approximation. For ease of cross-referencing to the shock-stage classification scheme for felsic rocks of Stöfler et al. (2018), we also provide a shock-stage estimate in Figure 2 and in subsequent, more detailed figures.

The intensity of the shock-metamorphic overprint documented in the recovered samples generally decreases with increasing distance from the impacted surfaces. The impacted surfaces show shallow, circular indentations of ~ 1 mm depth and ~ 10 mm width (e.g., Figure 3). Immediately recognizable on the macroscopic scale is a lens-shaped zone of intense fragmentation and grain-size reduction that, in both recovered samples, extends up to depths that correspond to about 3 GPa (Figures 2a and 3). This lens is absent in the unshocked reference sample (Figure S2 in Supporting Information S1). Fractures within and on the sides of these lenses are similar to those described by Hörz (1969) and Polansky and Ahrens (1990). Specifically, concentric as well as radial fractures exist in the samples' interiors whereas spall fractures and near-surface fractures exist close to the impacted surfaces. Additionally, side-spallation fractures exist at the sides, but not the bottoms, of the shocked granite cylinders. These are a result of the geometry of the sample and the titanium container and are therefore not further discussed here. While an in-depth analysis of shock-induced fragmentation is beyond the scope of this article, a typical succession of deformation microfabrics in the recovered samples is shown in Figures 4a–4c. Material compressed to <1 GPa exhibits fractures of hundreds of micrometers length that typically follow grain boundaries (Figure 2a and Figure S5 in Supporting Information S1). Such fractures are generally absent in the unshocked reference sample (Figure 4a and Figure S2 in Supporting Information S1). Fractures in material compressed to between 1 and 3 GPa are more numerous and shorter and either follow grain boundaries or penetrate grains (Figure 4b). The number of grain-penetrating fractures tends to increase with decreasing distance from the point of impact. In addition, tensile fractures that created porosity exist in this region (Figure 2a and Figure S4 in Supporting Information S1). Material compressed to >3 GPa shows abundant intragranular fractures and significantly smaller fragment sizes; moreover, gouge-like deformation bands in which grain sizes are typically on the order of $5 \mu\text{m}$ first exist between 3 and 6 GPa (Figure 3).

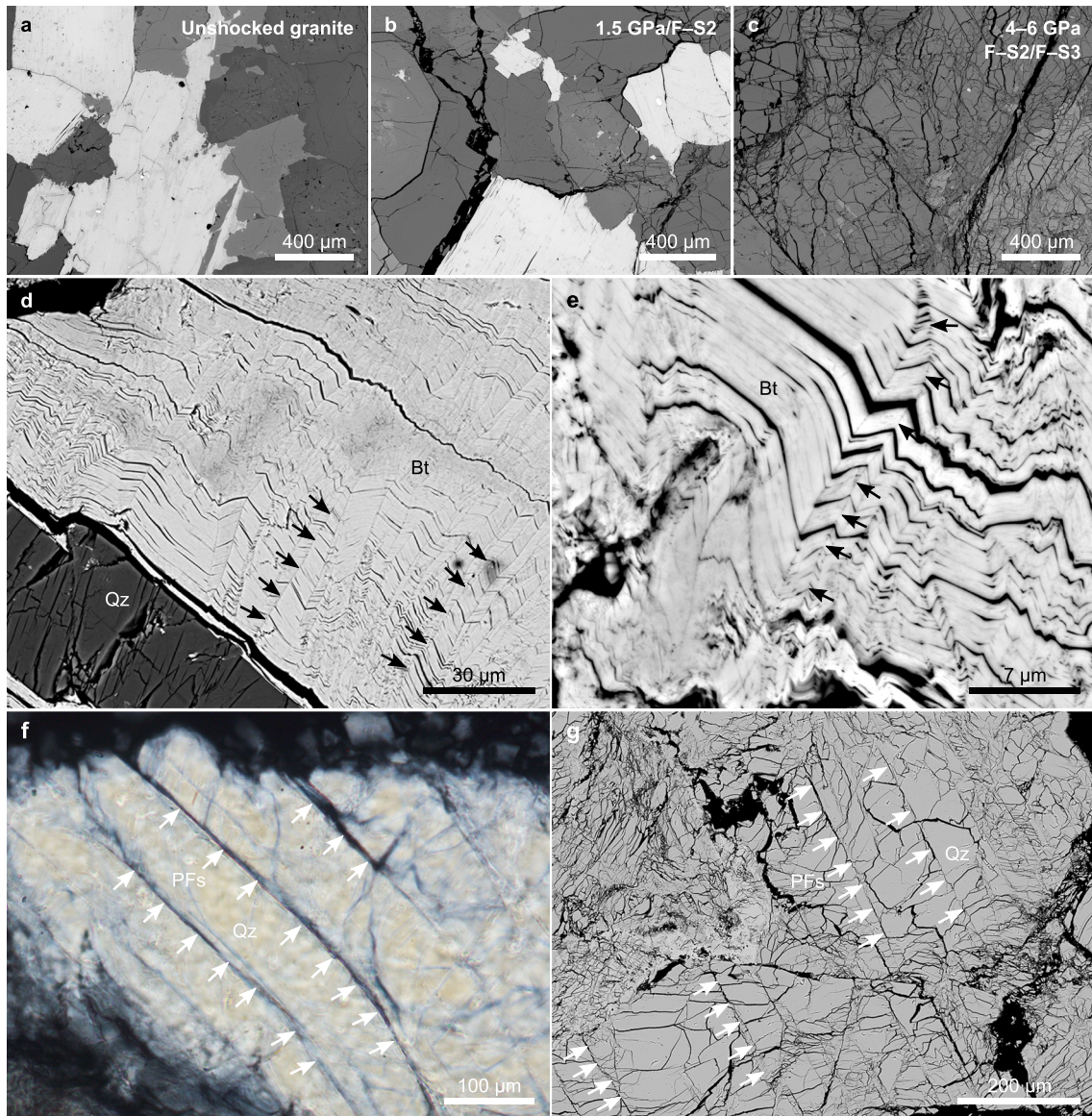


Figure 4. Representative images of fragmentation and stage F-S2/F-S3 (~5–10 GPa) shock metamorphism. (a–c) Representative back-scattered electron (BSE) images of increasingly intense fragmentation and grain-size reduction observed at different depths in the shocked granite cylinder recovered from experiment #494 compared against the unshocked reference sample. (d and e) Representative BSE images of kink bands (arrows) in biotite (Bt). (f) Optical micrograph (crossed polarizers) of bent planar fractures (PFs; arrows) in quartz (Qz). (g) Backscattered electron image of PFs in quartz (arrows) cross-cut by a network of microfractures.

In addition to fragmentation, solid-state deformation of minerals appears in regions compressed to ≥ 4 GPa (Figure 3). Typically, kink bands in biotite (Figures 4d and 4e) are observed here, whereas the remaining mineral phases of the granite are fractured, but otherwise show no shock-metamorphic overprint. Undulatory extinction in quartz and the feldspars first exists in regions compressed to about 5–8 GPa. The first *sensu stricto* shock effects observed in the shocked granite are planar fractures (PFs) in quartz, which are present in regions compressed to >5 GPa, but are best developed in material compressed to ≥ 10 GPa (Figures 4f and 4g; Figure S6a in Supporting Information S1). They typically occur in the form of a set of several parallel, straight PFs with (0001) , $\{10\bar{1}1\}$, or $\{11\bar{2}0\}$ orientations per grain, but seemingly “curved” or “bent” PFs were also observed (Figure 4f). Typically, PFs are cut by an irregular network of fractures (Figure 4g) and often extend across whole grains, but PFs that terminate within grains were also observed. Planar deformation features (PDFs) abundantly occur in quartz compressed to >10 –12 GPa and typically consist of two intersecting sets (Figures 5a and 5b; Figure S6b in Supporting Information S1) with $\{11\bar{2}1\}$ and $\{11\bar{2}2\}$ orientations. A detailed petrographic study of PFs, PDFs,

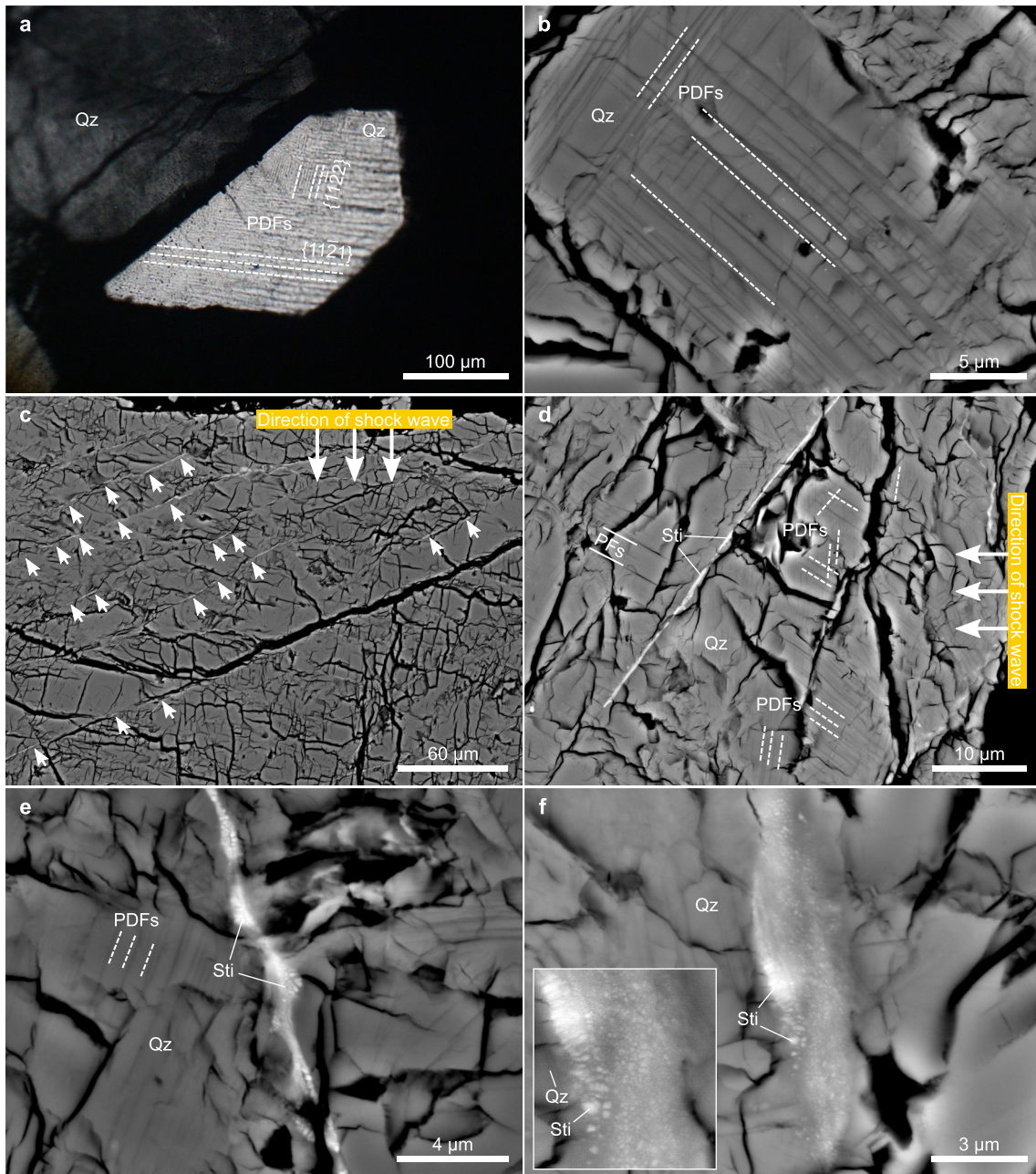


Figure 5. Representative images of stage F-S3 to F-S4 (~15–18 GPa) shock metamorphism. (a) Optical micrograph (crossed polarizers) and (b) back-scattered electron (BSE) image of planar deformation features (PDFs, highlighted by stippled lines) in heavily fractured quartz (Qz). (c) Overview BSE image of heavily fractured, PDF-bearing quartz with narrow veins of stishovite (highlighted by arrows) oriented at about 45° to the direction of shock-wave propagation. (d–f) Detailed views (BSE images) of veins containing stishovite (Sti) in heavily shocked and fractured quartz.

and feather features observed in these experiments will be given in a separate study that is currently available in abstract form (Tada et al., 2022).

Quartz near the impacted surfaces and at depths that correspond to ≥ 10 –12 GPa contains in both experiments numerous veins of 1–3 μm thickness and 20–80 μm length that are significantly brighter in BSE images than the surrounding quartz (Figures 5c and 5d). These veins typically occur in the form of several parallel sets that are oriented at $\sim 45^\circ$ to the direction of shock-wave propagation (Figures 5c and 5d). High-magnification BSE images (Figures 5e and 5f) reveal that the veins consist of individual, about 50–400-nm-wide crystallites set in a matrix that appears slightly darker than the surrounding quartz (Figure 5f). The surrounding quartz typically

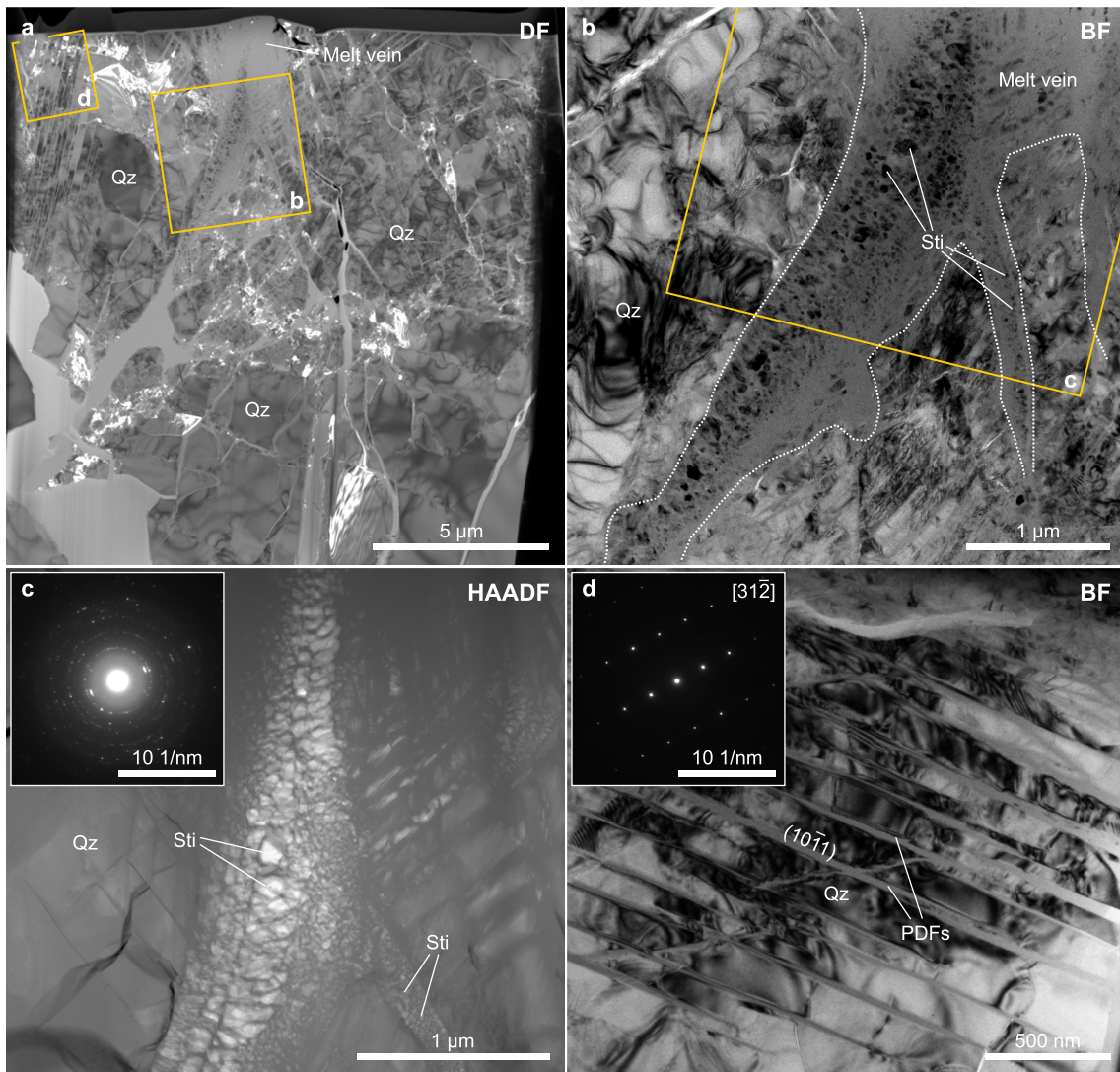


Figure 6. Characteristics of polycrystalline stishovite in quenched melt veins. (a) Low-magnification dark-field scanning transmission electron microscopy (STEM) image of a focused ion beam foil cut across a melt vein in planar deformation feature (PDF)-bearing, heavily fractured quartz (Qz). (b, c) Bright-field (BF) transmission electron microscopy (TEM) and high-angle annular dark-field STEM images, respectively, of stishovite (Sti) nanocrystals in the melt vein. The selected area electron diffraction (SAED) pattern shown in the inset of (c) was obtained from within the melt vein and confirms the presence of stishovite nanocrystals (reflected as a series of rings) in amorphous SiO_2 (reflected by the diffuse gray background within the innermost ring); note that a few reflections originate from nearby quartz. (d) A representative BF TEM image of PDFs in quartz. The SAED pattern shown in the inset was obtained from one of the quartz laths and can be indexed to a zone axis of $[31\bar{2}]$. The PDFs are oriented nearly on $(10\bar{1}1)$.

shows two or three sets of well-developed PDFs and numerous microfractures (Figures 5d and 5e). All EDS point analyses obtained from these veins were consistent with pure silica (Table S4 in Supporting Information S1). A representative melt vein with adjacent, PDF-bearing quartz was characterized by TEM (Figure 6a). The grain size of crystallites in the vein, as visible in TEM, ranged from about 150 nm down to a few nanometers, and the nanocrystallites are set in a matrix of amorphous SiO_2 (Figures 6b and 6c). Representative SAED patterns obtained from the nanocrystallites (inset in Figure 6c) revealed d -spacings that are fully compatible with stishovite, while additional reflections could be assigned to adjacent quartz (Table 2). Stishovite grains occur at the vein border in a palisade-like fashion and are usually irregularly shaped. Their orientation is variable, yielding almost continuous electron diffraction rings, which are similar to Debye-Scherrer rings observed in the case of granular media. Furthermore, the amorphous nature of the planar lamellae in adjacent quartz was confirmed in TEM-BF images (Figure 6d). Typical lamellae are between 10 and 30 nm across and the orientation of the lamellae in quartz close to the vein (Figures 6a and 6d) is parallel to a plane of the rhombohedral form $\{10\bar{1}1\}$. The

Table 2
List of Observed Bragg Reflections (d_{obs}) in the Selected Area Electron Diffraction Pattern Obtained From the Melt Vein Shown in Figure 6c Compared Against Reference Values (d_{ref}) for Stishovite (Chao et al., 1962) and Quartz (Levien et al., 1980)

$hk(i)l$	d_{ref} (Å)	d_{obs} (Å)	Phase
0 1 -1 1	3.343	3.354	Quartz
1 1 0	1.959	2.955	Stishovite
1 0 1	2.246	2.245	Stishovite
1 1 1	1.981	1.981	Stishovite
2 1 0	1.870	1.849	Stishovite
0 2 -2 2	1.672	1.676	Quartz
2 1 1	1.530	1.533	Stishovite
2 2 0	1.478	1.471	Stishovite
0 2 -2 3/2 0 -2 3/0 3 -3 1	1.375	1.375	Quartz
3 1 0	1.322	1.321	Stishovite
1 1 2	1.215	1.237	Stishovite
3 1 1	1.185	1.188	Stishovite
2 0 2	1.123	1.123	Stishovite

thickness as well as orientation of the amorphous lamellae is typical for PDFs formed in quartz in the pressure range achieved in our experiments (Stöffler & Langenhorst, 1994).

3.3. Localized Melting

High-magnification, transmitted-light photomicrographs and BSE images reveal a network of glassy veins in material beneath the impacted surfaces that we interpret as quenched silicate melts (Figure 7). The melt veins are typically 5–20 μm across (Figure 7) and reach lengths of several hundred micrometers (Figure 3). Melt veins typically exist along former grain boundaries (e.g., between quartz and plagioclase as shown in Figures 7a and 7b or between biotite and quartz as shown in Figure 7c), but grain-penetrating melt veins, for example, within quartz, were also detected (Figures 7d–7f). Both vesicle-free glasses (e.g., Figure 7b) as well as vesicular glasses (e.g., Figures 7c and 7e) were observed. Occasionally, the glass veins contain rounded mineral clasts (predominantly quartz; Figure 7e) as well as schlieren of variable brightness in BSE images (Figure 7f) that indicate mixing of melts of variable chemical composition. This interpretation is substantiated by EDS point analyses (Figure 8; Table S4 in Supporting Information S1), which suggest that both monomineralic (e.g., quartz) and polymineralic (e.g., mixtures of quartz and feldspar) melts exist.

The locations of the melt veins are mapped in Figure 3 onto the overview BSE images. The calculated peak pressure and temperature distributions suggest that the melt veins predominantly formed in material that was compressed to between 6 and 18 GPa and heated, on average, to peak temperatures of 400–770 K. Peak volumetric strain rates in these regions are estimated by the models to $\sim 0.3 \times 10^6$ – $5 \times 10^6 \text{ s}^{-1}$. However, in experiment #505, a short grain-interface melt vein was detected in a deformation band in material nominally compressed to about 4 GPa and heated to about 350 K. In experiment #494, similar melt veins extend to depths that correspond to about 5.5 GPa and 400 K. At the overview scale of Figure 3, it also becomes apparent that the melt veins are often, but not exclusively, located along prominent fractures or deformation bands that are characterized by grain-size reduction due to intense comminution (Figures 7a–7d). This holds especially true for experiment #505, in which the dominant deformation band that extends from the impacted surface to the lower right in Figure 3b is decorated by an almost continuous melt film.

4. Discussion

We have provided evidence of local melting in initially non-porous granite at far lower peak-pressure thresholds than currently considered in shock-classification schemes or numerical models. As will be outlined below, we argue that melting of granite dynamically compressed in shock-recovery experiments with spherically decaying compressing pulses was caused by highly localized shear deformation, which also resulted in the comminution of mineral grains along highly localized deformation bands. Our findings of stishovite in melt veins close to the impacted surfaces further suggest that localized frictional melting of small volumes of the host phase is a prerequisite for the formation of a high-pressure polymorph in melt veins. Moreover, rapid quenching of the high-pressure polymorphs below a critical temperature and before the pressure returns to ambient conditions is required to avoid back transformation to low-pressure polymorphs. These findings strengthen views that “shock” veins containing high-pressure polymorphs in moderately shocked meteorites represent shear-induced melts from which high-pressure polymorphs nucleated at high pressure. We ultimately argue that the occurrence of highly localized melt veins as well as trace amounts of stishovite should be added to the list of consultable diagnostic shock effects in the F–S3 shock stage for felsic crystalline rocks of Stöffler et al. (2018). We will outline these conclusions in more detail below.

4.1. Shear-Induced Melting

The dominant occurrence of melt veins along deformation bands of intense grain comminution suggests that melting was caused by highly localized shear deformation. This is consistent with the numerical models, which

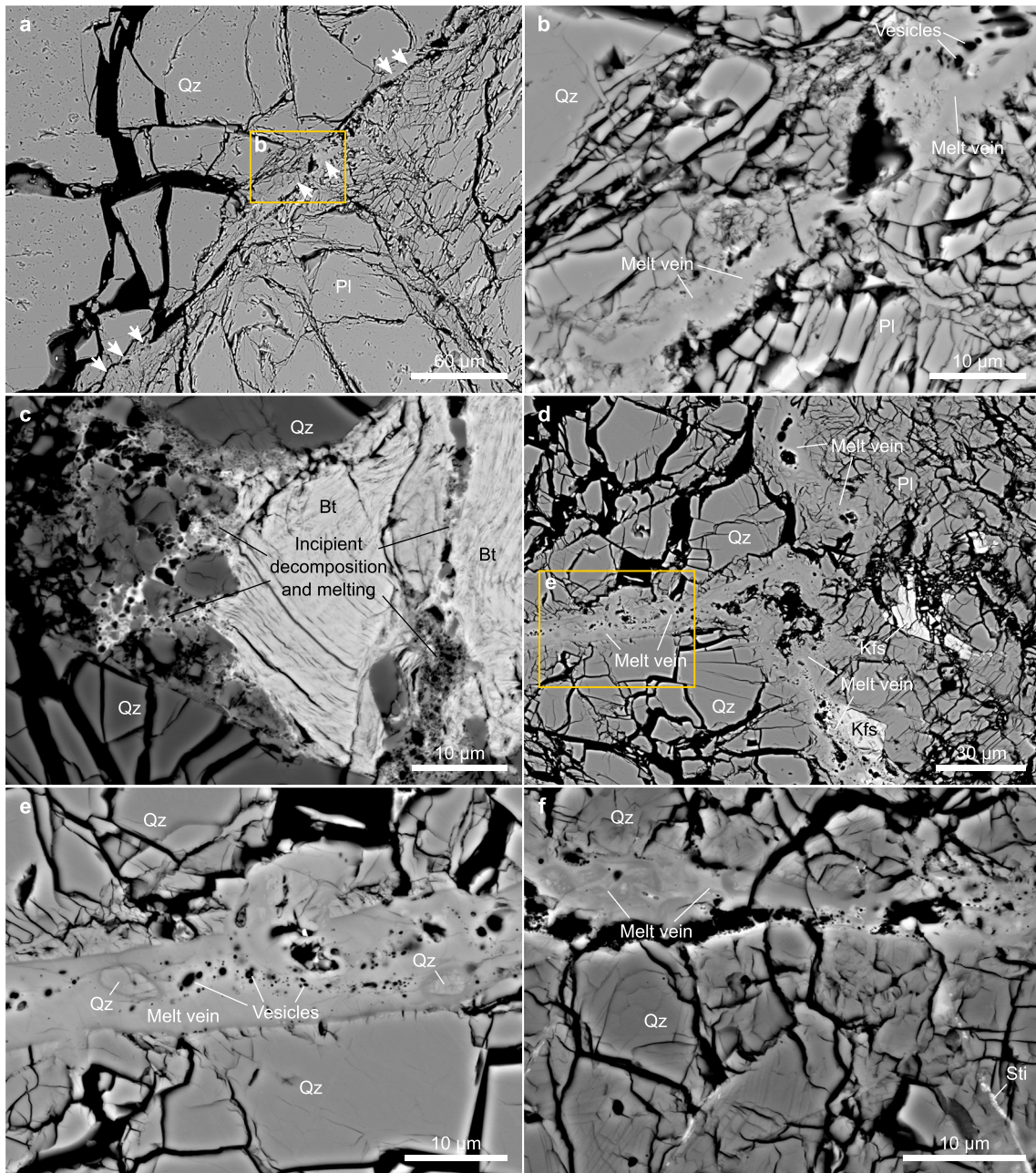


Figure 7. Representative back-scattered electron (BSE) images of quenched melt veins in granite of shock stage F–S2 to F–S3/F–S4. (a, b) Thin melt film along a grain boundary between quartz (Qz) and plagioclase (Pl). Note the intense comminution of plagioclase. (c) Decomposition or incipient melting of biotite (Bt) enclosed in quartz. Note again the intense comminution of quartz close to the biotite grain. (d, e) Several melt veins formed along former grain boundaries between plagioclase, alkali feldspar (Kfs), and quartz. Note the occurrence of vesicles as well as mineral clasts in the melt vein. (f) Melt vein formed in heavily fractured quartz with planar deformation features. Note the thin vein of stishovite (Sti) in the lower right corner. The schlieren in the melt vein, reflected by slightly different BSE intensity, reflects mixing of melts of different compositions (cf. Figure 8).

show that peak pressures (4–18 GPa) and temperatures (350–770 K) were far too low to cause incipient whole-rock melting of granite upon decompression from a shocked state high enough on the Hugoniot to pass the solid–liquid phase-boundaries of the granite’s constituents, which should require >60 GPa (e.g., Stöffler et al., 2018, and references therein). Given the rather similar densities of the major granite components and the absence of initial pore space, we can largely exclude that these melts formed from local pressure amplifications due to impedance contrasts among grains of significantly different densities (Ogilvie et al., 2011; Wittmann et al., 2021) or at interfaces between rock and air-filled porosity (Kowitz et al., 2013). As outlined in Text S1 and Figure S4 in

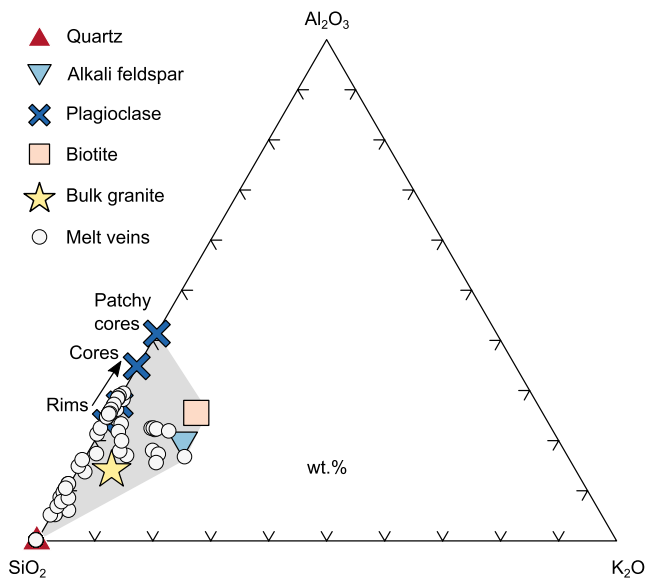


Figure 8. Chemical compositions of the melt veins (energy-dispersive X-ray spectroscopy data; cf. Table S4 in Supporting Information S1) as well as of quartz, alkali feldspar, plagioclase, and biotite (wavelength-dispersive X-ray spectroscopy data; cf. Table S1 in Supporting Information S1) in the unshocked reference sample plotted in SiO_2 - Al_2O_3 - K_2O composition space. The gray field in the background illustrates theoretically possible melt compositions obtained by simple mixing of monomineralic melts. The bulk composition of the granite (micro X-ray fluorescence spectroscopy data) is given for reference. While some data point at monomineralic melts derived from quartz or the feldspars, the majority of data is consistent with mixing of monomineralic quartz and plagioclase melts as well as plagioclase and alkali feldspar melts. Textural evidence for melt mixing is given in Figure 7f.

Supporting Information S1 and due to the rather similar shock impedances, local peak-pressure amplification will be negligible for neighboring quartz and feldspar, but considerable in cases where a high-density mineral (e.g., biotite, zircon) is enclosed within minerals of lower density (e.g., quartz). Based on the approach outlined in Wittmann et al. (2021), we estimate that peak-pressure fluctuations between quartz and the feldspars due to impedance effects will be much less than ± 2 GPa for an average peak pressure of 18 GPa. This pressure amplification would still be too low (Stöffler & Langenhorst, 1994; Stöffler et al., 2018) to facilitate incipient melting of essentially single-crystal quartz or feldspar along grain boundaries (Figures 7a and 7b) upon decompression from the shocked state, making an additional heat-producing mechanism necessary. Similarly, we estimate that impedance effects between quartz shocked to 18 GPa and biotite result in local amplification of shock pressure in biotite to 25 ± 1 GPa, which would still be too low (Stöffler et al., 2018) to have caused the observed grain-boundary melting of biotite enclosed in quartz (Figure 7c) during unloading. In addition, we observed melt veins that are neighbored by the same material (e.g., left part of Figure 7d) or which formed within fragmented quartz grains (Figure 7f). These examples further demonstrate that local excursions in shock pressure caused by impedance effects cannot account for the observed melting. The models, however, suggest that peak volumetric strain rates experienced in the targets' subsurface were high enough (on the order of 10^6 s^{-1}) to cause friction-induced melting (e.g., Spray, 1998).

Indeed, notwithstanding differences in chemical composition, the observed melt veins are similar to “shock” veins in numerous meteorites (e.g., Langenhorst & Poirier, 2000; Sharp & De Carli, 2006; Stöffler et al., 1991; Tomioka & Miyahara, 2017; Tomioka et al., 2016). Notwithstanding differences in scale, they are also similar to S-type pseudotachylites or pseudotachylitic breccias known from the terrestrial impact-crater record (e.g., Reimold, 1995; Reimold et al., 2015; Spray, 1995, 1998; Spray

& Thompson, 1995; L. M. Thompson & Spray, 1994). However, the most striking natural counterparts to the experimentally produced melt veins described here are thin melt veins about 1–500 μm across that contain majorite, a high-pressure polymorph of garnet, in shocked crystalline basement of the Steen River impact structure in Canada (Walton et al., 2016). The melt veins described by Walton et al. (2016) occur in plagioclase–orthoclase–quartz–amphibole–biotite gneiss shock-compressed to about 14–20 GPa, which is comparable to the shock pressure ranges reached in granite in our experiments. Formation of these melt veins by shear-induced friction melting was considered the most plausible cause by Walton et al. (2016). The results of our experiments are consistent with this interpretation and suggest that shear-induced melting at low to moderate bulk peak pressures can be significant in shocked crystalline basement. Melt veins formed in moderately shocked host materials were also observed, and shown to be caused by shear heating, in previous experiments with simple analog materials (e.g., Kenkmann et al., 2000; Langenhorst et al., 2002).

While shear-induced melting in impact scenarios is a well-known process, our experiments shed light onto the onset, petrologic context, and spatial distribution of shear-induced melting in complex, non-porous, felsic silicate rocks subjected to intense shear deformation during shock compression and release. Our experiments further show that shear deformation will be heterogeneously distributed in the shocked target and that melt veins formed by shear will form along deformation bands or areas of intense comminution that are also heterogeneously distributed in the target. This finding is in agreement to the damage and deformation models of Collins et al. (2004), which predict that strain is heterogeneously distributed, resulting in localized failure of rock; the deformation bands observed here can be regarded as evidence for highly localized, non-uniform failure (cf. Grady, 1980; D. R. Schmitt & Ahrens, 1989). Although no statistical analysis of fragment-size distributions of the deformation bands and the surrounding fractured granite was performed, BSE images obtained from the deformation bands (e.g., Figures 7b, 7d, and 7e) suggest that there is a transition between pure comminution (forming gouge with fragment sizes on the order of a few micrometers) and shear melting (forming melt veins). This view is consistent

with the conceptual model of Spray (1995) and petrographic descriptions of “shock” veins in meteorites (e.g., Tomioka & Miyahara, 2017; Tomioka et al., 2016) and thin melt veins in terrestrial pseudotachylitic breccias (e.g., Reimold, 1995; Reimold et al., 2015; Spray, 1995, 1998; Spray & Thompson, 1995; L. M. Thompson & Spray, 1994). Moreover, our results suggest that highly localized heating due to fault-like shear deformation may occur in addition to the recently investigated effect of “bulk” post-shock heating due to plastic deformation (Kurosawa & Genda, 2018; Quintana et al., 2015; Wakita et al., 2022).

As a caveat, we must stress that shock fronts in natural impact events have a planar instead of spherical geometries on the scale of individual millimeter-sized grains; as a result of this planar geometry, the majority of naturally shock-metamorphosed material experiences much less intense shear deformation than produced in our experiments. Given the appreciation of these limitations, our results nevertheless clearly illustrate the generation of intense local heating in cases where a significant shear component is involved during cratering. The shear-induced melt veins described by Walton et al. (2016) from moderately shocked crystalline basement of the Steen River impact structure are probably the strongest proponents of this conclusion. In addition, our observations of the onset and mode of shear-induced melting have relevance for the interpretation of “shock” veins found in meteorites. Specifically, our observations suggest that shear-induced melting of otherwise only moderately shocked host material may indeed be the favorable formation mechanism for such melt veins, strengthening recent arguments put forward by Hu and Sharp (2022).

4.2. Formation of Stishovite

For both experiments investigated here, the presence of stishovite is restricted to amorphous veins that occur in volumetrically dominant, shocked and fractured quartz close to the impacted surfaces, that is, in material that experienced >10–12 GPa (Figure 3). The pressure threshold for the onset of stishovite formation determined here is, thus, consistent with previous studies (e.g., De Carli & Milton, 1965; Fazio et al., 2018; Kleeman & Ahrens, 1973; Mansfeld et al., 2017). The $\sim 45^\circ$ orientation of the stishovite-containing veins relative to the direction of shock-wave propagation is also consistent with previous experiments conducted with planar shock waves (D. R. Schmitt & Ahrens, 1989). However, the occurrence of stishovite in shocked quartz is currently attributed to the F–S4 and F–S5 shock stage of Stöfler et al. (2018), which are assigned to >20 and >35 GPa, respectively. Our results suggest that the occurrence of minor amounts of stishovite should be added to the F–S3 shock stage as well.

Similar stishovite-bearing amorphous veins were produced in shock-recovery experiments with porous sandstone at 7.5 and 12.5 GPa and were interpreted as silica melts from which stishovite crystallized rapidly at pressure (Mansfeld et al., 2017). In addition, such veins were also reported from shock-metamorphosed (shock stage F–S3 to F–S4), quartz-rich gneisses from the Ries impact structure, Germany (Stähle et al., 2008) and from pseudotachylites at the Vredefort impact structure, South Africa (e.g., Martini, 1991). Stähle et al. (2008) suggested that stishovite nucleated at an early stage of the loading process from a high-pressure frictional melt at high (~ 3300 K) temperature and moderate (<30 GPa) shock pressure. The palisade-like texture of stishovite at the vein borders observed here (Figure 6c) suggests incipient crystallization from the rim and proceeding from there into the melt vein, consistent with the conceptual model of D. R. Schmitt and Ahrens (1989) and the observations of Stähle et al. (2008). In keeping with the phase diagram of silica (e.g., Mansfeld et al., 2017), we argue that stishovite formed as a stable liquidus phase from silica melt at elevated pressure. Where quenching of the melt was too fast to crystallize stishovite, we observed silica glass as a final product. In addition, where peak pressures were below ~ 10 GPa, the nucleation of stishovite did not occur and the silica melt quenched to lechatelierite, as illustrated by the stishovite-free melt veins at greater depths in the targets (Figures 3 and 7). Taken together, these observations suggest that localized frictional melting of small volumes of the host phase is a prerequisite for the formation of a high-pressure polymorph in “shock” veins, whereas rapid quenching of the high-pressure polymorph below a critical temperature and before the pressure returns to ambient conditions is required to avoid back transformation to low-pressure polymorphs. Although our experiments involved much smaller scales, both in terms of physical dimensions as well as shock-pulse durations, than natural impact events, stishovite-bearing veins in PDF-bearing, partially diaplectic quartz in shocked granitoid gneisses from the Ries impact structure (Stähle et al., 2008) have similar physical dimensions (i.e., less than a few micrometers across) and mineral assemblages (e.g., stishovite nanocrystallites set in amorphous matrix) to the veins produced here. Moreover, high-pressure polymorphs found in “shock” veins in ordinary chondrites and lunar,

Martian, and howardite–eucrite–diogenite meteorites are typically also located at or on vein boundaries (for a review, see Tomioka & Miyahara, 2017). Notwithstanding differences in bulk composition and mineralogy, our results suggest that high-pressure polymorphs associated with “shock” veins in shocked meteorites are the result of crystallization of mono- or polymineralic, likely friction-induced melts under high pressure. The similarity between the experimentally produced melt veins and their natural counterparts in the Ries impactites (Stähle et al., 2008), in the shocked crystalline basement at Steen River (Walton et al., 2016), and in shocked meteorites (e.g., Langenhorst & Poirier, 2000; Sharp & De Carli, 2006; Stöffler et al., 1991; Tomioka & Miyahara, 2017; Tomioka et al., 2016) illustrates the applicability of our experiments to the interpretation of naturally produced shock effects. We deem that elimination of multiple ring-up compression from our experimental setup—the biggest culprit that plagued conventional shock-recovery experiments—and the use of a singular, spherically decaying compressive pulse are key to simulate the impact process more faithfully. Confidence in laboratory scale investigations of shock metamorphism using singular shock compression has furthermore been inspired by, for example, comparisons of impact melting of sandstone in laboratory experiments and natural terrestrial impact craters (Ebert et al., 2013; Hamann et al., 2013, 2018) and recent petrographic observations on impactites from the Kamil impact structure (e.g., Folco et al., 2018), which are similar to, and confirmed predictions from, shocked samples from shock-wave experiments (e.g., Kowitz et al., 2013).

4.3. Implications for Schemes of Progressive Shock Metamorphism

Our results illustrate that stishovite-bearing melt veins occur in otherwise only moderately shock-metamorphosed granite that experienced significantly lower peak pressures (~4–18 GPa) than those envisaged to result in impact melting of dense, non-porous granite (>50–65 GPa). As local pressure hotspots due to impedance contrasts between neighboring phases of different densities (Ogilvie et al., 2011; Wittmann et al., 2021) or at interfaces between rock and air-filled porosity (e.g., Kowitz et al., 2013) can be excluded here as causes for localized melting, we concluded that the melt veins result from highly localized, shear-induced heating that formed in comparatively cold, moderately shocked material. While some of the classification schemes (e.g., for chondrites or mafic silicate rocks) advocated by Stöffler et al. (2018) consider shock effects resulting from local excursions in peak pressure or temperatures, some others, among them the scheme concerned with felsic rocks, currently do not consider such effects. Based on our observations, we argue that incipient melting along shear zones must be added to the shock classification scheme for felsic rocks in a similar manner as it has been done for chondrites or mafic silicate rocks (cf. Tables 5 and 8 of Stöffler et al. (2018)). Our experiments suggest that the onset of localized melting of granite starts within the F–S3 shock stage, consistent with the onset of localized melting and melt-vein formation in chondrites and mafic rocks at the C–S3 and M–S3 shock stages, respectively. Our results further suggest that the occurrence of minor amounts of stishovite should be added to the F–S3 shock stage as well.

5. Conclusions

We report on shock-recovery experiments that produce decaying hemispherical shock fronts in granite. These allowed us to petrographically investigate progressive shock metamorphism of granite dynamically compressed to between 0.5 and 18 GPa. Our combination of a hemispherical shock-wave configuration, numerical modeling of shock states, and the possibility to recover and investigate entire shocked samples furthermore allowed us to investigate the significance of shear-induced melting during shock metamorphism. We found that progressive shock metamorphism of granite observed here is mostly consistent with current classification schemes of shock metamorphism of felsic magmatic rocks. Specifically, kink bands in biotite start to appear at ~4 GPa; undulatory extinction in quartz and feldspar starts at ~5 GPa; PFs in quartz appear above ~5–8 GPa; and PDFs in quartz appear above ~10–12 GPa. However, we observed thin amorphous veins with either quartz-like or quartz-feldspar-like compositions in areas of intense comminution and at peak pressures as low as ~6 GPa that are inconsistent with current views of the onset of shock-induced melting in non-porous felsic rocks at >60 GPa. We interpret these as quenched melts that formed by highly localized shear deformation. Amorphous veins in quartz grains shock-compressed to between 10 and 18 GPa contain stishovite nanocrystallites that crystallized from silica melt at high pressure. Based on these observations, we argue that the occurrence of highly localized, shear-induced melt veins and of trace amounts of stishovite should be added to the list of diagnostic shock effects in the F–S3 shock stage for felsic crystalline rocks of Stöffler et al. (2018). Taken together, our results provide significant insight into the shock processes in granite and, by extension, other non-porous crystalline rocks that

experience intense shear deformation during singular shock compression as in natural hypervelocity impacts. Ultimately, our findings suggest that melt veins containing high-pressure polymorphs in the terrestrial cratering record (S-type pseudotachylites) and in shocked meteorites (“shock” veins) are the result of shear-induced friction heating during shock loading or subsequent unloading combined with quenching of friction-generated melt at high pressure.

Data Availability Statement

The iSALE shock physics code is not fully open-source but is distributed on a case-by-case basis to academic users in the impact community for non-commercial use. A description of the application requirements can be found at the iSALE website (<https://isale-code.github.io/terms-of-use.html>). All other data presented in this study and the Supporting Information S1 are available in an online repository at <https://doi.org/10.5281/zenodo.7881492> (Hamann et al., 2023).

References

- Amsden, A., Ruppel, H., & Hirt, C. (1980). SALE: A simplified ALE computer program for fluid flow at all speeds (Los Alamos National Laboratories Report LA-8095).
- Barrat, J.-A., Chaussidon, M., Yamaguchi, A., Beck, P., Villeneuve, J., Byrne, D. J., et al. (2021). A 4,565-My-old andesite from an extinct chondritic protoplanet. *Proceedings of the National Academy of Sciences of the United States of America*, 118(11), e2026129118. <https://doi.org/10.1073/pnas.2026129118>
- Bell, M. S. (2016). CO₂ release due to impact devolatilization of carbonate: Results of shock experiments. *Meteoritics & Planetary Science*, 51(4), 619–646. <https://doi.org/10.1111/maps.12613>
- Chao, E. C. T., Fahey, J. J., Littler, J., & Milton, D. J. (1962). Stishovite, SiO₂, a very high pressure new mineral from Meteor Crater, Arizona. *Journal of Geophysical Research*, 67(1), 419–421. <https://doi.org/10.1029/JZ0671001p00419>
- Collins, G. S., Elbeshhausen, D., Davison, T. M., Wünnemann, K., Ivanov, B. A., & Melosh, H. J. (2016). iSALE-Dellen manual. *Figshare*, 10, m9. <https://doi.org/10.6084/m9.figshare.3473690.v2>
- Collins, G. S., Melosh, H. J., & Ivanov, B. A. (2004). Modeling damage and deformation in impact simulations. *Meteoritics & Planetary Science*, 39(2), 217–231. <https://doi.org/10.1111/j.1945-5100.2004.tb00337.x>
- De Carli, P. S., & Milton, D. J. (1965). Stishovite: Synthesis by shock wave. *Science*, 147(3654), 144–145. <https://doi.org/10.1126/science.147.3654.144>
- Ebert, M., Hecht, L., Deutsch, A., & Kenkmann, T. (2013). Chemical modification of projectile residues and target material in a MEMIN cratering experiment. *Meteoritics & Planetary Science*, 48(1), 134–149. <https://doi.org/10.1111/j.1945-5100.2012.1429.x>
- Ebert, M., Poelchau, M. H., Kenkmann, T., Gulick, S. P. S., Hall, B., Lofi, J., et al. (2021). Comparison of stress orientation indicators in Chicxulub's peak ring: Kinked biotites, basal PDFs, and feather features. In W. U. Reimold & C. Koeberl (Eds.), *Large meteorite impacts and planetary evolution VI: Geological society of America special paper 550* (pp. 479–493). [https://doi.org/10.1130/2021.2550\(21\)](https://doi.org/10.1130/2021.2550(21))
- Ebert, M., Poelchau, M. H., Kenkmann, T., & Schuster, B. (2020). Tracing shock-wave propagation in the Chicxulub crater: Implications for the formation of peak rings. *Geology*, 48(8), 814–818. <https://doi.org/10.1130/G47129.1>
- Fazio, A., Pollok, K., & Langenhorst, F. (2018). Experimental evidence for mechanical Brazil twins as an indicator of low-pressure shock metamorphism (<17.5 GPa). *Geology*, 49(9), 787–790. <https://doi.org/10.1130/G40198.1>
- Folco, L., Mugnaioli, E., Gemelli, M., Masotta, M., & Campanale, F. (2018). Direct quartz-coesite transformation in shocked porous sandstone from Kamil Crater (Egypt). *Geology*, 46(9), 739–742. <https://doi.org/10.1130/G45116.1>
- Grady, D. E. (1980). Shock deformation of brittle solids. *Journal of Geophysical Research*, 85(B2), 913–924. <https://doi.org/10.1029/JB085iB02p00913>
- Hamann, C., Fazio, A., Ebert, M., Hecht, L., Wirth, R., Folco, L., et al. (2018). Silicate liquid immiscibility in impact melts. *Meteoritics & Planetary Science*, 53(8), 1594–1632. <https://doi.org/10.1111/maps.12907>
- Hamann, C., Hecht, L., Ebert, M., & Wirth, R. (2013). Chemical projectile–target interaction and liquid immiscibility in impact glass from the Wabar craters, Saudi Arabia. *Geochimica et Cosmochimica Acta*, 121, 291–310. <https://doi.org/10.1016/j.gca.2013.07.030>
- Hamann, C., Kurosawa, K., Ono, H., Tada, T., Langenhorst, F., Pollok, K., et al. (2023). Experimental evidence for shear-induced melting and generation of stishovite in granite at low (<18 GPa) shock pressure [Dataset]. <https://doi.org/10.5281/zenodo.7881492>
- Hamann, C., Stöffler, D., & Reimold, W. U. (2016). Interaction of aluminum projectiles with quartz sand in impact experiments: Formation of khatyrkite (CuAl₂) and reduction of SiO₂ to Si. *Geochimica et Cosmochimica Acta*, 192, 295–317. <https://doi.org/10.1016/j.gca.2016.07.018>
- Holland, T., & Powell, R. (2001). Calculation of phase relations involving haplogranitic melts using an internally consistent thermodynamic dataset. *Journal of Petrology*, 42(4), 673–683. <https://doi.org/10.1093/ptrology/42.4.673>
- Hörz, F. (1969). Structural and mineralogical evaluation of an experimentally produced impact crater in granite. *Contributions to Mineralogy and Petrology*, 21(4), 365–377. <https://doi.org/10.1007/BF02672808>
- Hörz, F., Cintala, M. J., See, T. H., & Le, L. (2005). Shock melting of ordinary chondrite powders and implications for asteroidal regoliths. *Meteoritics & Planetary Science*, 40(9–10), 1329–1346. <https://doi.org/10.1111/j.1945-5100.2005.tb00404.x>
- Hu, J., & Sharp, T. G. (2022). Formation, preservation and extinction of high-pressure minerals in meteorites: Temperature effects in shock metamorphism and shock classification. *Progress in Earth and Planetary Science*, 9(1), 6. <https://doi.org/10.1186/s40645-021-00463-2>
- Ivanov, B. A., Deniem, D., & Neukum, G. (1997). Implementation of dynamic strength models into 2-D hydrocodes: Applications for atmospheric breakup and impact cratering. *International Journal of Impact Engineering*, 20(1–5), 411–430. [https://doi.org/10.1016/S0734-743X\(97\)87511-2](https://doi.org/10.1016/S0734-743X(97)87511-2)
- Kenkmann, T., Hornemann, U., & Stöffler, D. (2000). Experimental generation of shock-induced pseudotachylites along lithological interfaces. *Meteoritics & Planetary Sciences*, 35(6), 1275–1290. <https://doi.org/10.1111/j.1945-5100.2000.tb01516.x>
- Kleeman, J. D., & Ahrens, T. J. (1973). Shock-induced transition of quartz to stishovite. *Journal of Geophysical Research*, 78(26), 5954–5960. <https://doi.org/10.1029/JB078i026p05954>
- Kohout, T., Petrova, E. V., Yakovlev, G. A., Grokhovsky, V. I., Penttilä, A., Maturilli, A., et al. (2020). Experimental constraints on the ordinary chondrite shock darkening caused by asteroid collisions. *Astronomy & Astrophysics*, 639, A146. <https://doi.org/10.1051/0004-6361/202037593>

Acknowledgments

We dedicate this study to the late Profs. Takafumi Matsui and Dieter Stöffler, who tremendously inspired and encouraged us to think outside the box and critically question established views. We thank Sanna Alwmark and Steven Jaret for constructive reviews and Bradley Thomson for editorial handling. Preparation of petrographic thin sections by Karen Helm-Knapp and assistance in the preparation of the BSE image mosaics by Felix Kaufmann are greatly appreciated. We thank Auriol Rae and Tom Sharp for fruitful discussions. We furthermore thank the developers of iSALE, including Gareth Collins, Kai Wünnemann, Boris Ivanov, Jay Melosh, and Dirk Elbeshhausen. We also thank Tom Davison for the development of pySALEPlot. This research was supported by JSPS KAKENHI Grant JP19H00726. C.H. was supported by a grant from MfN's Innovation Fund. K.K. is also supported by JSPS KAKENHI Grants JP18H0092, JP19H00726, JP21H01140, and JP21K18660. F.L. thanks the Deutsche Forschungsgemeinschaft for granting the electron microscopic facilities via the Gottfried-Wilhelm Leibniz programme (LA830/14-1). Open Access funding enabled and organized by Projekt DEAL.

- Kowitz, A., Güldemeister, N., Reimold, W. U., Schmitt, R. T., & Wünnemann, K. (2013). Diaplectic quartz glass and SiO₂ melt experimentally generated at only 5 GPa shock pressure in porous sandstone: Laboratory observations and meso-scale numerical modeling. *Earth and Planetary Science Letters*, *384*, 17–26. <https://doi.org/10.1016/j.epsl.2013.09.021>
- Kraus, R. G., Stewart, S. T., Swift, D. C., Bolme, C. A., Smith, R. F., Hamel, S., et al. (2012). Shock vaporization of silica and the thermodynamics of planetary impact events. *Journal of Geophysical Research*, *117*(E9), E09009. <https://doi.org/10.1029/2012JE004082>
- Kurosawa, K., & Genda, H. (2018). Effects of friction and plastic deformation in shock-comminuted damaged rocks on impact heating. *Geophysical Research Letters*, *45*(2), 620–626. <https://doi.org/10.1002/2017GL076285>
- Kurosawa, K., Ohno, S., Sugita, S., Mieno, T., Matsui, T., & Hasegawa, S. (2012). The nature of shock-induced calcite (CaCO₃) devolatilization in an open system investigated using a two-stage light gas gun. *Earth and Planetary Science Letters*, *337*(338), 68–76. <https://doi.org/10.1016/j.epsl.2012.05.022>
- Kurosawa, K., Ono, H., Niihara, T., Sakaiya, T., Kondo, T., Tomioka, N., et al. (2022). Shock recovery with decaying compressive pulses: A shock effect in calcite (CaCO₃) around the Hugoniot elastic limit. *Journal of Geophysical Research*, *127*(6), e2021JE007133. <https://doi.org/10.1029/2021JE007133>
- Langenhorst, F., & Deutsch, A. (1994). Shock experiments on pre-heated α- and β-quartz: I. Optical and density data. *Earth and Planetary Science Letters*, *125*(1–4), 407–420. [https://doi.org/10.1016/0012-821X\(94\)90229-1](https://doi.org/10.1016/0012-821X(94)90229-1)
- Langenhorst, F., & Deutsch, A. (2012). Shock metamorphism of minerals. *Elements*, *8*(1), 31–36. <https://doi.org/10.2113/gselements.8.1.31>
- Langenhorst, F., & Poirier, J.-P. (2000). Anatomy of black veins in Zagami: Clues to the formation of high-pressure phases. *Earth and Planetary Science Letters*, *184*(1), 37–55. [https://doi.org/10.1016/S0012-821X\(00\)00317-4](https://doi.org/10.1016/S0012-821X(00)00317-4)
- Langenhorst, F., Poirier, J.-P., Deutsch, A., & Hornemann, U. (2002). Experimental approach to generate shock veins in single crystal olivine by shear melting. *Meteoritics & Planetary Science*, *37*(11), 1541–1553. <https://doi.org/10.1111/j.1945-5100.2002.tb00809.x>
- Levien, L., Prewitt, C. T., & Weidner, D. J. (1980). Structure and elastic properties of quartz at pressure. *American Mineralogist*, *65*, 920–930.
- Mansfeld, U., Langenhorst, F., Ebert, M., Kowitz, A., & Schmitt, R. T. (2017). Microscopic evidence of stishovite generated in low-pressure shock experiments on porous sandstone: Constraints on its Genesis. *Meteoritics & Planetary Science*, *52*(7), 1449–1464. <https://doi.org/10.1111/maps.12867>
- Martini, J. E. J. (1991). The nature, distribution and Genesis of the coesite and stishovite associated with the pseudotachylite of the Vredefort Dome, South Africa. *Earth and Planetary Science Letters*, *103*(1–4), 285–300. [https://doi.org/10.1016/0012-821X\(91\)90167-G](https://doi.org/10.1016/0012-821X(91)90167-G)
- Melosh, H. J. (1989). *Impact cratering: A geologic process*. Oxford University Press.
- Millot, M., Dubrovinskaya, N., Černok, A., Blaha, S., Dubrovinsky, L., Braun, D. G., et al. (2015). Shock compression of stishovite and melting of silica at planetary interior conditions. *Science*, *347*(6220), 418–420. <https://doi.org/10.1126/science.1261507>
- Milton, D. J., & De Carli, P. S. (1963). Maskelynite: Formation by explosive shock. *Science*, *140*(3567), 670–671. <https://doi.org/10.1126/science.140.3567.670>
- Miyahara, M., Tomioka, N., & Bindi, L. (2021). Natural and experimental high-pressure, shock-produced terrestrial and extraterrestrial materials. *Progress in Earth and Planetary Science*, *8*(1), 59. <https://doi.org/10.1186/s40645-021-00451-6>
- Nagaki, K., Kadono, T., Sakaiya, T., Kondo, T., Kurosawa, K., Hironaka, Y., et al. (2016). Recovery of entire shocked samples in a range of pressure from ~100 GPa to Hugoniot elastic limit. *Meteoritics & Planetary Science*, *51*(6), 1153–1162. <https://doi.org/10.1111/maps.12654>
- Ogilvie, P., Gibson, R. L., Reimold, W. U., Deutsch, A., & Hornemann, U. (2011). Experimental investigation of shock metamorphic effects in a metapelitic granulite: The importance of shock impedance contrast between components. *Meteoritics & Planetary Science*, *46*(10), 1565–1586. <https://doi.org/10.1111/j.1945-5100.2011.01250.x>
- Ono, H., Kurosawa, K., Niihara, T., Mikouchi, T., Tomioka, N., Isa, J., et al. (2023). Experimentally shock-induced melt veins in basalt: Improving the shock classification of eucrites. *Geophysical Research Letters*, *50*(1), e2022GL101009. <https://doi.org/10.1029/2022GL101009>
- Osinski, G. R., Grieve, R. A. F., Ferrière, L., Losiak, A., Pickersgill, A. E., Cavosie, A. J., et al. (2022). Impact Earth: A review of the terrestrial impact record. *Earth-Science Reviews*, *232*, 104112. <https://doi.org/10.1016/j.earscirev.2022.104112>
- Pierazzo, E., Vickery, A. M., & Melosh, H. J. (1997). A reevaluation of impact melt production. *Icarus*, *127*(2), 408–423. <https://doi.org/10.1006/icar.1997.5713>
- Polansky, C. A., & Ahrens, T. J. (1990). Impact spallation experiments: Fracture patterns and spall velocities. *Icarus*, *87*(1), 140–155. [https://doi.org/10.1016/0019-1035\(90\)90025-5](https://doi.org/10.1016/0019-1035(90)90025-5)
- Quintana, S. N., Crawford, D. A., & Schultz, P. H. (2015). Analysis of impact melt and vapor production in CTH for planetary applications. *Procedia Engineering*, *103*, 499–506. <https://doi.org/10.1016/j.proeng.2015.04.065>
- Rae, A. S. P., Collins, G. S., Morgan, J. V., Salge, T., Christeson, G. L., Leung, J., et al. (2019). Impact-induced porosity and microfracturing at the Chicxulub impact structure. *Journal of Geophysical Research: Planets*, *124*(7), 1960–1978. <https://doi.org/10.1029/2019JE005929>
- Rae, A. S. P., Kenkmann, T., Padmanabha, V., Poelchau, M. H., Schäfer, F., Dörfler, M. A., & Müller, L. (2022). Dynamic compressive strength and fragmentation in sedimentary and metamorphic rocks. *Tectonophysics*, *824*, 229221. <https://doi.org/10.1016/j.tecto.2022.229221>
- Rae, A. S. P., Poelchau, M. H., & Kenkmann, T. (2021). Stress and strain during shock metamorphism. *Icarus*, *370*, 114687. <https://doi.org/10.1016/j.icarus.2021.114687>
- Reimold, W. U. (1995). Pseudotachylite in impact structures — Generation by friction melting and shock brecciation?: A review and discussion. *Earth-Science Reviews*, *39*(3–4), 247–265. [https://doi.org/10.1016/0012-8252\(95\)00033-X](https://doi.org/10.1016/0012-8252(95)00033-X)
- Reimold, W. U., Fischer, L., Müller, J., Kenkmann, T., Schmitt, R.-T., Altenberger, U., & Kowitz, A. (2015). Impact-generated pseudotachylitic breccia in drill core BH-5 Hättberg, Siljan impact structure, Sweden. *GFF*, *137*(2), 141–162. <https://doi.org/10.1080/11035897.2015.1015264>
- Riller, U., Poelchau, M. H., Rae, A. S. P., Schultz, F. M., Collins, G. S., Melosh, H. J., et al. (2018). Rock fluidization during peak-ring formation of large impact structures. *Nature*, *562*(7728), 511–518. <https://doi.org/10.1038/s41586-018-0607-z>
- Schaal, R. B., & Hörz, F. (1977). Shock metamorphism of lunar and terrestrial basalts. In *Proceedings 8th Lunar Science Conference* (pp. 1697–1729).
- Schmitt, D. R., & Ahrens, T. J. (1989). Shock temperatures in silica glass: Implications for modes of shock-induced deformation, phase transformation, and melting with pressure. *Journal of Geophysical Research*, *94*(B5), 5851–5871. <https://doi.org/10.1029/JB094iB05p05851>
- Schmitt, R. T. (2000). Shock experiments with the H6 chondrite Kernouvé: Pressure calibration of microscopic shock effects. *Meteoritics & Planetary Science*, *35*(3), 545–560. <https://doi.org/10.1111/j.1945-5100.2000.tb01435.x>
- Sharp, T. G., & De Carli, P. S. (2006). Shock effects in meteorites. In D. S. Lauretta & H. Y. McSween (Eds.), *Meteorites and the early solar system II* (pp. 653–677). University of Arizona Press.
- Spray, J. G. (1995). Pseudotachylite controversy: Fact or friction? *Geology*, *23*(12), 1119–1122. [https://doi.org/10.1130/0091-7613\(1995\)023%3C1119:PCFOF%3E2.3.CO;2](https://doi.org/10.1130/0091-7613(1995)023%3C1119:PCFOF%3E2.3.CO;2)
- Spray, J. G. (1998). Localized shock- and friction-induced melting in response to hypervelocity impact. In M. M. Grady, R. Hutchinson, G. J. H. McCall, & D. A. Rothery (Eds.), *Meteorites: Flux with time and impact effects* (Vol. 40, pp. 195–204). Geological Society.

- Spray, J. G., & Thompson, L. M. (1995). Friction melt distribution in a multi-ring impact basin. *Nature*, 373(6510), 130–132. <https://doi.org/10.1038/373130a0>
- Srinivasan, P., Dunlap, D. R., Agee, C. B., Wadhwa, M., Coleff, D., Ziegler, K., et al. (2018). Silica-rich volcanism in the early solar system dated at 4.565 Ga. *Nature Communications*, 9(1), 3036. <https://doi.org/10.1038/s41467-018-05501-0>
- Stähle, V., Altherr, R., Koch, M., & Nasdala, L. (2008). Shock-induced growth and metastability of stishovite and coesite in lithic clasts from suevite of the Ries impact crater (Germany). *Contributions to Mineralogy and Petrology*, 155(4), 457–472. <https://doi.org/10.1007/s00410-007-0252-2>
- Stöffler, D., Hamann, C., & Metzler, K. (2018). Shock metamorphism of planetary silicate rocks and sediments: Proposal for an updated classification system. *Meteoritics & Planetary Science*, 53(1), 5–49. <https://doi.org/10.1111/maps.12912>
- Stöffler, D., Keil, K., & Scott, E. R. D. (1991). Shock metamorphism of ordinary chondrites. *Geochimica et Cosmochimica Acta*, 55(12), 3845–3867. [https://doi.org/10.1016/0016-7037\(91\)90078-J](https://doi.org/10.1016/0016-7037(91)90078-J)
- Stöffler, D., & Langenhorst, F. (1994). Shock metamorphism of quartz in nature and experiment: I. Basic observation and theory. *Meteoritics*, 29(2), 155–181. <https://doi.org/10.1111/j.1945-5100.1994.tb00670.x>
- Tada, T., Kurosawa, K., Ono, H., Hamann, C., Okamoto, T., Niihara, T., & Matsui, T. (2022). Shock recovery of granite with a decaying shock wave: Feather features formation in quartz. In *Paper presented at the 53rd Lunar and Planetary Science Conference*.
- Terada, K., & Bischoff, A. (2009). Asteroidal granite-like magmatism 4.53 Gyr ago. *The Astrophysical Journal*, 699(2), L68–L71. <https://doi.org/10.1088/0004-637X/699/2/L68>
- Thompson, L. M., & Spray, J. G. (1994). Pseudotachylitic rock distribution and Genesis within the Sudbury impact structure. In B. O. Dressler, R. A. F. Grieve, & V. L. Sharpton (Eds.), *Large meteorite impacts and planetary evolution* (Vol. 293, pp. 275–287). Geological Society of America.
- Thompson, S. L., & Lauson, H. S. (1972). Improvements in the Chart-D radiation hydrodynamic code III: Revised analytical equation of state (SC-RR-71 0714 Sandia Laboratories).
- Tomeoka, K., Yamahana, Y., & Sekine, T. (1999). Experimental shock metamorphism of the Murchison CM carbonaceous chondrite. *Geochimica et Cosmochimica Acta*, 63(21), 3683–3703. [https://doi.org/10.1016/S0016-7037\(99\)00149-0](https://doi.org/10.1016/S0016-7037(99)00149-0)
- Tomioka, N., & Miyahara, M. (2017). High-pressure minerals in shocked meteorites. *Meteoritics & Planetary Science*, 52(9), 2017–2039. <https://doi.org/10.1111/maps.12902>
- Tomioka, N., Miyahara, M., & Ito, M. (2016). Discovery of natural MgSiO₃ tetragonal garnet in a shocked chondritic meteorite. *Science Advances*, 2(3), e1501725. <https://doi.org/10.1126/sciadv.1501725>
- Tracy, S. J., Turneaure, S. J., & Duffy, T. S. (2020). Structural response of α -quartz under plate-impact shock compression. *Science Advances*, 6(35), eabb3913. <https://doi.org/10.1126/sciadv.abb3913>
- Wakita, S., Genda, H., Kurosawa, K., Davison, T. M., & Johnson, B. C. (2022). Effect of impact velocity and angle on deformational heating and postimpact temperature. *Journal of Geophysical Research*, 127(8), e2022JE007266. <https://doi.org/10.1029/2022JE007266>
- Walton, E. L., Sharp, T. G., & Hu, J. (2016). Frictional melting processes and the generation of shock veins in terrestrial impact structures: Evidence from the Steen River impact structure, Alberta, Canada. *Geochimica et Cosmochimica Acta*, 180, 256–270. <https://doi.org/10.1016/j.gca.2016.02.024>
- Wittmann, A., Cavosie, A. J., Timms, N. E., Ferrière, L., Rae, A., Rasmussen, C., et al. (2021). Shock impedance amplified impact deformation of zircon in granitic rocks from the Chicxulub impact crater. *Earth and Planetary Science Letters*, 575, 117201. <https://doi.org/10.1016/j.epsl.2021.117201>
- Wünnemann, K., Collins, G. S., & Melosh, H. J. (2006). A strain-based porosity model for use in hydrocode simulations of impacts and implications for transient crater growth in porous targets. *Icarus*, 180(2), 514–527. <https://doi.org/10.1016/j.icarus.2005.10.013>
- Wünnemann, K., Zhu, M.-H., & Stöffler, D. (2016). Impacts into quartz sand: Crater formation, shock metamorphism, and ejecta distribution in laboratory experiments and numerical models. *Meteoritics & Planetary Science*, 51(10), 1762–1794. <https://doi.org/10.1111/maps.12710>
- Yuan, F., & Prakash, V. (2013). Plate impact experiments to investigate shock-induced inelasticity in Westerly granite. *International Journal of Rock Mechanics and Mining Sciences*, 60, 277–287. <https://doi.org/10.1016/j.ijrmm.2012.12.024>
- Zeng, X., Li, X., Xia, X.-P., Liu, J., Cui, Z., Yu, W., & Ouyang, Z. (2021). New evidence for 4.32 Ga ancient silicic volcanism on the Moon. *Geophysical Research Letters*, 48(13), e2021GL092639. <https://doi.org/10.1029/2021GL092639>

References From the Supporting Information

- Ahrens, T. J., & Johnson, M. L. (1995). Shock wave data for minerals. In T. J. Ahrens (Ed.), *Mineral physics and crystallography, A handbook of physical constants* (pp. 143–183). American Geophysical Union.
- Marsh, S. P. (1980). *LASL shock Hugoniot data*. University of California Press.
- Sekine, T., Duffy, T. S., Rubin, A. M., Anderson, W. W., & Ahrens, T. J. (1995). Shock compression and isentropic release of granite. *Geophysical Journal International*, 120(2), 247–261. <https://doi.org/10.1111/j.1365-246X.1995.tb01817.x>
- Sugita, S., & Schultz, P. H. (2003). Interactions between impact-induced vapor clouds and the ambient atmosphere: 2. Theoretical modeling. *Journal of Geophysical Research*, 108(E6), 5052. <https://doi.org/10.1029/2002JE001960>
- Tillotson, J. H. (1962). Metallic equations of state for hypervelocity impact. (Technical Report GA-3216).
- Trunin, R. F., Gudarenko, L. F., Zhernokletov, M. V., & Simakov, G. V. (2001). *Experimental data on shock compression and adiabatic expansion of condensed matter*. Russian Federal Nuclear Center.